

GEOMETRY-PRESERVING NUGGED ELASTIC BAND AND DIMER METHODS UNDER ANISOTROPIC FORCE UNCERTAINTY

YIFAN YU* AND YANGSHUAI WANG†

Abstract. The nudged elastic band (NEB) and Dimer methods are standard tools for computing minimum-energy paths and index-one saddle points in atomistic transition problems. They are increasingly driven by surrogate or learned force models, whose force errors are often anisotropic and spatially varying near transition states and defect cores, where saddle-search iterations are most sensitive. We introduce uncertainty-aware NEB and Dimer methods (UA-NEB, UA-Dimer) that use covariance as an optimizer-level reliability metric while preserving the mean-potential saddle-search equations: an oblique normal projection for NEB and covariance-weighted rotation and translation for Dimer. Both algorithms fit Robbins–Monro recursions; under a local Lyapunov stability hypothesis, verified explicitly for a canonical UA-NEB setting and stated as a hypothesis for UA-Dimer, the stochastic iterations converge almost surely within the corresponding local stability neighborhood. In the analytic benchmark, UA-NEB reduces mean barrier error by 21% relative to stochastic NEB and UA-Dimer reduces the reflected-gradient residual by 22%; in the 127-atom tungsten-vacancy benchmark, full UA-NEB reduces mean barrier error by 56% relative to stochastic NEB and by 23% relative to diagonal covariance weighting. These results show that anisotropic uncertainty is most useful when embedded in the constrained geometry of the optimizer rather than collapsed into a scalar acquisition or trust criterion.

Key words. nudged elastic band, Dimer method, uncertainty quantification, stochastic approximation, crystalline defects, active learning

MSC codes. 65C20, 65K10, 65C30, 60H35, 70F45, 82D25

1. Introduction. Atomistic transition rates depend exponentially on index-one saddle barriers [36]: an error of a few millielectronvolts can shift a predicted rate by tens of percent. Such barriers govern activated events in crystals, molecules, and catalysts, making accurate saddle search central to predictive kinetics. The nudged elastic band (NEB) method [18, 14, 15] and Dimer method [13, 10] are standard tools for this task. In large-scale searches, however, the optimizer often queries stochastic, ensemble, surrogate, or learned forces rather than exact deterministic forces. Machine-learned interatomic potentials (MLIPs) [1, 2, 4, 38, 16] are one important instance, providing mean forces and anisotropic, spatially inhomogeneous covariance estimates that are often largest near defects and transition states. For crystalline-defect calculations, adaptive QM/MM coupling and elastic far-field analysis provide complementary ways to control spatial and modeling errors [37, 28].

This creates a constrained-algorithm design problem, not only a modeling problem. The *geometry* of NEB and Dimer is the structure that makes them saddle-search methods rather than generic descent methods: NEB separates normal physical forces from tangential image redistribution, while Dimer couples a curvature-direction solve with a reflected-gradient translation. These projections, tangent spaces, reflections, and zero sets encode the deterministic saddle problem. A covariance preconditioner that is harmless for unconstrained gradient descent can be harmful here, because it need not commute with the normal–tangential decomposition and may move the stationary set from the minimum-energy path of the mean potential to a metric-distorted one. Thus covariance should inform the step geometry without changing the equations

*Department of Mathematics, Faculty of Science, National University of Singapore, 10 Lower Kent Ridge Road, Singapore.

†Corresponding author. Department of Mathematics, Faculty of Science, National University of Singapore, 10 Lower Kent Ridge Road, Singapore (yswang@nus.edu.sg).

whose solution is being sought.

Existing uses of uncertainty in saddle-search computations mainly act outside this update geometry. GP-NEB constructs a probabilistic path surrogate [20, 19], and active-learning force-field algorithms use uncertainty to select configurations for high-fidelity labeling [30, 35, 21]; force uncertainty can also come from deep ensembles [23], Bayesian potentials [9], conformal or calibration-based UQ frameworks [16, 40], or atomistic uncertainty frameworks [29]. More broadly, randomized collocation and least-squares polynomial-chaos constructions [33, 12, 17, 11] and information-theoretic sensitivity bounds for stochastic dynamics [7, 34] provide complementary UQ tools for propagating or ranking uncertainty. These mechanisms are essential for reducing model bias, but they do not by themselves make each NEB or Dimer step direction-dependent in the local reliability of the force.

The distinction from GP-NEB is one of numerical setting rather than only implementation. GP-NEB is most natural when high-fidelity force evaluations are scarce and the Gaussian-process posterior itself is the path model. The present methods assume that a stochastic, ensemble, or learned force model already supplies repeated force queries together with a calibrated covariance estimate, and ask how that covariance should enter the constrained optimizer without changing the mean-potential target equations. Direct comparison with GP-NEB therefore depends on the surrogate class, training set, and cost of reference-force acquisition; here we isolate the optimizer-level covariance geometry.

Our design principle is to let covariance change the step metric, but not the stationarity equations defining the mean-potential saddle problem. For NEB, with $G = (\Sigma_F + \lambda I)^{-1}$, we replace the Euclidean normal projection by the oblique projection

$$Q_{\perp, G}z = z - G\tau \frac{\tau^\top z}{\tau^\top G\tau},$$

so that $Q_{\perp, G}G\nabla\bar{E} = 0$ is equivalent to the classical MEP condition $\nabla\bar{E} \parallel \tau$, not to a metric-shifted equation. For Dimer, whose reflected-gradient translation is full rank, the metric preconditions the reflected gradient and noisy rotational residual while preserving the critical-point set. We call the algorithms uncertainty-aware NEB (UA-NEB) and uncertainty-aware Dimer (UA-Dimer).

We make three contributions. First, we derive covariance-weighted UA-NEB and UA-Dimer updates that preserve the saddle-search targets. Second, we cast the iterations as Robbins–Monro recursions, prove local convergence under stated stability assumptions, and give an explicit canonical Lyapunov verification for UA-NEB. Third, we test the mechanism under controlled covariance models on an analytic saddle-search problem and a 127-atom bcc tungsten vacancy hop, using paired seeds and matched force-evaluation counts.

The rest of the paper is organized as follows. Section 2 fixes the deterministic and stochastic problem setting; Section 3 develops the UA-NEB and UA-Dimer algorithms together with the climbing and active-learning variants; Section 4 establishes the local convergence theory and the scalable covariance realizations; Section 5 reports the numerical experiments; Section 6 concludes.

Notation. Throughout, $\langle \cdot, \cdot \rangle$ and $\|\cdot\|$ denote the Euclidean inner product and norm, and I denotes the identity matrix. For a nonzero vector a , $aa^\top / \|a\|^2$ is the Euclidean rank-one projection onto $\text{span}\{a\}$ and $P_a := I - aa^\top / \|a\|^2$ is the corresponding orthogonal complement projection; in particular, for a unit Dimer direction v , $P_v = I - vv^\top$. Expectations and variances are taken with respect to the randomness in the force and

covariance queries made up to the current iteration. Metric-dependent projections, weighted norms, residuals, and NEB/Dimer spacings are introduced where they first appear, in §3 and §4.

2. Problem setting. We work in a mass-weighted, or otherwise preconditioned, configuration $x \in \mathbb{R}^d$ after removing rigid translations, fixed atoms, and imposed linear constraints. Two energies are kept distinct. The high-fidelity potential E_\star defines the physical barrier, while \bar{E} denotes the posterior, ensemble, or surrogate mean energy seen by the optimizer. The algorithms in this paper seek saddles and minimum-energy paths of \bar{E} ; covariance estimates do not define a new target energy, but instead quantify which force directions are reliable enough to use in a numerical step.

For later comparison with physical barriers, harmonic transition-state theory [36] gives $k(T) = \nu^\dagger(T) \exp[-(E_\star(x_\star^\dagger) - E_\star(a))/k_B T]$, where x_\star^\dagger is the high-fidelity saddle and ν^\dagger is a Hessian-eigenvalue prefactor. A barrier error δ therefore shifts the rate by

$$(2.1) \quad k_\delta(T)/k(T) = \exp[-\delta/k_B T],$$

so a 10 meV error gives a rate shift of about 21% at 600 K and 47% at 300 K. The numerical experiments therefore report barrier errors directly, rather than only residual norms. We next recall the deterministic NEB and Dimer equations, then specify the stochastic force and covariance interface.

2.1. Deterministic saddle-search background. Let $E : \mathbb{R}^d \rightarrow \mathbb{R}$ be a smooth deterministic potential and let a, b be two local minimizers. In the algorithms below this deterministic target is $E = \bar{E}$. A minimum energy path (MEP) is characterized by the vanishing of the force normal to the path. In the continuum notation, $\varphi : [0, 1] \rightarrow \mathbb{R}^d$, with $\varphi(0) = a$ and $\varphi(1) = b$, satisfies

$$(2.2) \quad (I - \tau\tau^\top)\nabla E(\varphi(s)) = 0, \quad \tau(s) = \frac{\varphi'(s)}{\|\varphi'(s)\|},$$

away from critical points. A highest point on a generic MEP is an index-one saddle x^\dagger , $\nabla E(x^\dagger) = 0$, with exactly one negative Hessian eigenvalue. Stability of the continuous MEP and convergence of discrete MEP approximations have recently been analyzed in [25, 24].

2.1.1. NEB. NEB [18, 14] discretizes a path from a to b by fixed endpoints $x_0 = a$, $x_{n+1} = b$, and interior images x_1, \dots, x_n . For an interior image, τ_i denotes the discrete tangent *estimator*. We use the energy-weighted rule of [14]. Under this rule, the tangent is chosen from the forward and backward secants $\Delta_i^\pm = x_{i\pm 1} - x_i$, with an energy-weighted combination near local energy extrema, and then unit-normalized. We denote this standard mapping by

$$(2.3) \quad \tau_i = \mathcal{T}_i(x_{i-1}, x_i, x_{i+1}; E).$$

This choice avoids the common corner-cutting and sliding-down instabilities of the original tangent rule; in the small-spacing limit on a smooth MEP, $\tau_i \rightarrow \tau(s)$ of (2.2).

The deterministic NEB force on an interior image is

$$(2.4) \quad \mathcal{F}_i^{\text{NEB}} = -(I - \tau_i\tau_i^\top)\nabla E(x_i) + k_s(\|x_{i+1} - x_i\| - \|x_i - x_{i-1}\|)\tau_i,$$

The normal component of the physical force relaxes the band onto the MEP, while the spring component distributes images along the path. A climbing-image modification removes the spring force and reverses the tangential true force on the image with largest energy [15]. Preconditioned MEP finders accelerate this deterministic relaxation by changing the path metric [26]; the covariance metric below has the different role of damping uncertain force directions while preserving (2.2).

The stochastic algorithms below preserve the MEP stationarity condition while replacing the Euclidean normal-force projection in (2.4) by covariance-weighted directions.

2.1.2. Dimer. The Dimer method [13, 10] seeks an index-one saddle without constructing an entire path. Given a center x and unit direction v , it estimates the Hessian action by a centered force difference. With the energy-Hessian convention,

$$(2.5) \quad \widehat{H}_h(x)v = -\frac{\widehat{F}(x+hv) - \widehat{F}(x-hv)}{2h}.$$

Here \widehat{F} denotes the queried force; in the deterministic case $\widehat{F} = F = -\nabla E$, while in the stochastic setting it is the oracle force specified in the next subsection. The orientation is rotated toward the lowest-curvature eigenvector by approximately minimizing the Rayleigh quotient $v^\top \nabla^2 E(x)v$ over $\|v\| = 1$. The center then moves along the reflected gradient

$$(2.6) \quad r_x(x, v) = -\nabla E(x) + 2vv^\top \nabla E(x),$$

which descends in directions orthogonal to v and ascends along v . Since independent force noise makes the variance of (2.5) scale like h^{-2} , the rotational step requires its own covariance weighting. Thus in both NEB and Dimer, covariance may change the metric of a step but not the deterministic equations that define the target MEP or saddle. Related saddle-search algorithms exploit MEP geometry, preconditioning, high-index saddle dynamics, or problem-specific nullspaces in other ways; examples include solution-landscape construction by generalized high-index saddle dynamics [39], spring-pair dynamics guided by the MEP tangent, and nullspace-preserving saddle search for ordered phase transitions with translational invariance [5, 6].

2.2. Stochastic force model and covariance estimation. The algorithms access \overline{E} through a stochastic force oracle. For a configuration $x \in \mathbb{R}^d$, the oracle returns

$$(2.7) \quad \widehat{F}(x, \omega) = -\nabla \overline{E}(x) + \zeta(x, \omega), \quad \mathbb{E}[\zeta | x] = 0, \quad \Sigma_F(x) = \text{Cov}[\zeta | x],$$

where ω labels model randomness, such as an ensemble member, bootstrap replica, posterior draw, or Gaussian-process sample. The covariance Σ_F may be obtained from ensemble or Bayesian force models [9, 23, 30, 21, 29]. Throughout we use the *energy-Hessian sign convention*: the physical force is $F = -\nabla E$, the gradient estimator is $\widehat{g} = -\widehat{F}$, and the Hessian-vector product is $\nabla^2 E v$. With this convention the centered-difference Hessian-vector product carries the minus sign in (2.5). A force-Jacobian convention would omit this sign; it is not used in the analysis.

The stochastic approximation target is the mean energy \overline{E} . The high-fidelity energy E_* enters through calibration, validation, and active learning, not through the deterministic drift of the optimizer. Let \mathcal{F}_k be the filtration generated by all force,

covariance, and active-learning decisions up to iteration k . For an adapted query x_k , define

$$(2.8) \quad \widehat{g}(x_k, \omega_{k+1}) = -\widehat{F}(x_k, \omega_{k+1}) = \nabla \overline{E}(x_k) - \zeta(x_k, \omega_{k+1}),$$

so $\mathbb{E}[\widehat{g}(x_k, \omega_{k+1}) \mid \mathcal{F}_k] = \nabla \overline{E}(x_k)$.

The algorithms below require only a calibrated covariance operator consistent with this conditional-moment model. Ensemble covariance is one common way to build such an operator. If ensemble energies are also available, the uncertainty of a reported barrier can be monitored directly, for example by $\text{Var}_m[E^{(m)}(x_c) - E^{(m)}(a)]$, where x_c is the reported barrier configuration. If a direct barrier variance is unavailable, one can instead use a linearized propagation of the available covariance information through the reported barrier functional; concrete operator-probing estimators are described in Supplementary Section SM5. These checks affect reporting and active-learning triggers, not the mean-potential target.

2.2.1. Calibrated ensemble covariance. Let $\{F^{(m)}(x)\}_{m=1}^M$ be force predictions from an independently seeded, bootstrapped, or posterior ensemble, and let

$$(2.9) \quad \bar{F}_M(x) = \frac{1}{M} \sum_{m=1}^M F^{(m)}(x).$$

The raw sample covariance is

$$(2.10) \quad \widehat{S}_M(x) = \frac{1}{M-1} \sum_{m=1}^M (F^{(m)}(x) - \bar{F}_M(x))(F^{(m)}(x) - \bar{F}_M(x))^\top.$$

The calibrated covariance used by the algorithms for a single-member stochastic query is

$$(2.11) \quad \widehat{\Sigma}_{FM}(x) = s_{\text{cal}}^2 \widehat{S}_M(x) + \sigma_{\text{floor}}^2 I,$$

where s_{cal} is a scalar or blockwise calibration factor obtained on a validation set and $\sigma_{\text{floor}} > 0$ prevents spuriously zero variance. If a force query averages several independent members, the covariance in (2.7) is replaced by the covariance of that averaged query; sampling one member per iteration gives (2.11) directly.

The raw ensemble covariance in (2.10) measures the spread of model predictions. Before it is interpreted as a force-error covariance, it should be calibrated against high-fidelity validation forces. We use the Gaussian negative-log-likelihood scaling s_{cal} , or a blockwise variant by atomic species, optionally combined with a coverage-based safety criterion. Finite ensembles can also produce noisy eigenvectors; when needed, we control this effect by a shrinkage parameter $\rho \in [0, 1]$ that blends the raw sample covariance with a block-sparse projection. The full calibration likelihood, coverage condition, and shrinkage formula are collected in Supplementary Section SM5. In the numerical experiments below the prescribed covariance is exact by construction, so we set $s_{\text{cal}} = 1$ and $\rho = 0$.

2.2.2. Operator realizations. For large d , the algorithms should not require a dense matrix. We assume the covariance module exposes the following operations:

$$(2.12) \quad z \mapsto \widehat{\Sigma}_F(x)z, \quad z \mapsto (\widehat{\Sigma}_F(x) + \lambda I)^{-1}z, \quad \log \det(\widehat{\Sigma}_F(x) + \lambda I),$$

and, when the log-determinant penalty is active, directional derivatives in arbitrary directions u ,

$$u^\top \nabla_x \log \det(\widehat{\Sigma}_F(x) + \lambda I).$$

The inverse operation can be exact for small blocks, a Woodbury apply for low rank, or a few Krylov iterations for sparse local covariances. This operator formulation is sufficient for the algorithms below, since the NEB and Dimer updates require only products of G with force-like vectors and scalar products such as $\tau^\top Gz$.

For a local or message-passing force model with finite effective interaction radius, epistemic uncertainty is often local in atomic environments even when the force itself is many-body. This motivates block or low-rank operator models such as

$$(2.13) \quad \Sigma_F(x) \approx \sum_{\ell=1}^L P_\ell^\top B_\ell(x) P_\ell,$$

where $P_\ell : \mathbb{R}^d \rightarrow \mathbb{R}^{b_\ell}$ extracts the Cartesian force components of a local atom cluster or defect-core patch, and $B_\ell \succeq 0$ is a small dense block. Overlapping blocks are allowed. A related low-rank form follows from local feature-gradient Jacobians:

$$(2.14) \quad \Sigma_F(x) \approx J_\theta(x) C_\theta J_\theta(x)^\top = U(x) C(x) U(x)^\top,$$

where C_θ is a posterior or ensemble covariance in parameter or latent-feature space. These forms are introduced here only as covariance interfaces for the algorithms. Detailed cost models and Woodbury or Krylov applies are deferred to §4.4 and Supplementary Section SM4; energy-only probing is described in Supplementary Section SM5; and the decomposition of barrier error into stochastic, optimization, and model terms is stated in Supplementary Proposition SM2.1.

3. Algorithms. The covariance interface of §2 gives directional reliability information, but it does not by itself say how that information should enter a constrained saddle-search algorithm. The design constraint in this section is therefore geometric: covariance may change the metric of a stochastic step, but it must not change the deterministic stationarity equations for the mean potential.

For NEB, the difficulty is a rank-deficient normal projection that does not commute with a generic covariance preconditioner. We resolve this with an oblique projection whose zero set is the classical MEP condition, then check local stability and the effect of a metric spring. For Dimer, the projection obstruction disappears, but the noisy Hessian-vector rotation and the reflected-gradient translation require separate covariance weights. The two constructions are different, but the organizing principle is the same: use uncertainty as step geometry, not as a new target energy. Throughout this section, $\epsilon > 0$ denotes a fixed small denominator regularization.

3.1. Uncertainty-aware NEB. Let x_i be an interior image. Given a regularization parameter $\lambda > 0$, define the reliability metric

$$(3.1) \quad G_i = G(x_i) := (\Sigma_F(x_i) + \lambda I)^{-1}.$$

Directions with high force uncertainty have smaller weight in the G_i metric and are damped in the preconditioned force. Since $(\lambda + \lambda_{\max}(\Sigma_F(x_i)))^{-1} I \preceq G_i \preceq \lambda^{-1} I$, the regularization λ keeps the inverse metric uniformly bounded even when the covariance estimator is rank deficient.

3.1.1. Weighted tangent and projections. The tangent component must be removed without shifting the MEP equation. For a gradient vector g , the Euclidean projection of $G_i g$ and the G_i -orthogonal projection both impose stationarity on a metric-shifted vector. We instead use the rank- $(d-1)$ projection whose range is the Euclidean normal subspace $\{z : \tau_i^\top z = 0\}$ and whose kernel is the metric tangent direction:

$$(3.2) \quad Q_{\perp, G_i}(z) = z - G_i \tau_i \frac{\tau_i^\top z}{\tau_i^\top G_i \tau_i}, \quad Q_{\parallel, G_i}(z) = G_i \tau_i \frac{\tau_i^\top z}{\tau_i^\top G_i \tau_i}.$$

This is an *oblique* projection: its range is the Euclidean tangent-orthogonal hyperplane and its kernel is $\text{span}\{G_i \tau_i\}$. Lemma 3.1 records the zero-set identity needed below.

LEMMA 3.1 (MEP-preserving projection identities). *Let G be symmetric positive definite and $\tau \neq 0$. The operators in (3.2) satisfy*

$$Q_{\perp, G}^2 = Q_{\perp, G}, \quad Q_{\parallel, G}^2 = Q_{\parallel, G}, \quad \tau^\top Q_{\perp, G} z = 0,$$

and $z = Q_{\perp, G} z + Q_{\parallel, G} z$. Moreover,

$$(3.3) \quad Q_{\perp, G} G g = 0 \iff (I - \tau \tau^\top / \|\tau\|^2) g = 0.$$

Proof. $\tau^\top Q_{\perp, G} z = \tau^\top z - \tau^\top G \tau \cdot \tau^\top z / (\tau^\top G \tau) = 0$. Idempotence follows since $Q_{\perp, G}^2 z = Q_{\perp, G} z - G \tau \cdot (\tau^\top Q_{\perp, G} z) / (\tau^\top G \tau) = Q_{\perp, G} z$, and analogously for $Q_{\parallel, G}$. For (3.3): if $Q_{\perp, G} G g = 0$, then $G g = G \tau (\tau^\top G g) / (\tau^\top G \tau)$, so $g \parallel \tau$; conversely, $g = c \tau$ gives $Q_{\perp, G} G g = c G \tau - c G \tau = 0$. \square

Remark 3.2 (Why the alternative projections fail). Euclidean projection of Gg and G -orthogonal projection both require $Gg \parallel \tau$, equivalently $g \parallel G^{-1} \tau$. Thus their zero set is a metric-shifted line unless τ is a G -eigenvector. A concrete 2×2 example is already decisive: take

$$\tau = e_1, \quad G = \begin{bmatrix} 7/4 & -3\sqrt{3}/4 \\ -3\sqrt{3}/4 & 13/4 \end{bmatrix}.$$

The classical zero set contains $g = e_1$, but $(I - \tau \tau^\top) G g = (0, -3\sqrt{3}/4)^\top \neq 0$. The competing projections instead select $g \parallel G^{-1} \tau \propto (13, 3\sqrt{3})^\top$, which is not parallel to τ . The oblique form (3.2) is used because $Q_{\perp, G} G g = 0$ is equivalent to the classical MEP condition $g \parallel \tau$. The extended comparison in Supplementary Section SM1, including Supplementary Figure S1, visualizes the corresponding flow geometry.

The metric also admits a constrained natural-gradient interpretation. Given a gradient sample g , the covariance-preconditioned normal force $-Q_{\perp, G} G g$ is the solution of

$$(3.4) \quad \begin{aligned} -Q_{\perp, G} G g &= \operatorname{argmin}_{\tau^\top s = 0} \left\{ g^\top s + \frac{1}{2} s^\top G^{-1} s \right\}, \\ &= \operatorname{argmin}_{\tau^\top s = 0} \|s + Gg\|_{G^{-1}}^2. \end{aligned}$$

Thus high-variance directions are damped before projection, while the deterministic MEP stationarity condition is unchanged. After computing Gg and $G\tau$, the projection in (3.2) requires only the scalar products $\tau^\top Gg$ and $\tau^\top G\tau$.

Lemma 3.1 is algebraic; the next statement gives the corresponding local dynamics. With fixed tangent, the oblique-force flow has the restricted energy as a Lyapunov function and is locally asymptotically stable at the constrained minimizer.

LEMMA 3.3 (Fixed-tangent local stability). *Fix a nonzero tangent τ and a symmetric positive definite metric G . Consider the constrained deterministic flow*

$$\dot{x} = -Q_{\perp,G}G\nabla\bar{E}(x), \quad \tau^\top(x - x_\star) = 0,$$

where x_\star is a nondegenerate constrained minimizer of \bar{E} on the affine hyperplane $\tau^\top(x - x_\star) = 0$. Then x_\star is a locally asymptotically stable equilibrium of the constrained flow. In particular, replacing the Euclidean normal force by the oblique covariance-weighted normal force changes the local metric and time scale, but not the constrained critical point.

Proof. The vector field is tangent to the hyperplane because $\tau^\top Q_{\perp,G}z = 0$ for every z . If $s = -Q_{\perp,G}G\nabla\bar{E}(x)$, then the variational identity (3.4) gives the KKT relation $G^{-1}s + \nabla\bar{E}(x) + \mu\tau = 0$ for some scalar μ . Since $\tau^\top s = 0$,

$$\nabla\bar{E}(x)^\top s = -s^\top G^{-1}s \leq 0.$$

Thus the restricted energy is a Lyapunov function. Near a nondegenerate constrained minimizer its restriction to the hyperplane is locally strongly convex, so the dissipation above gives local asymptotic stability. \square

Lemma 3.3 holds τ fixed. In the running iteration τ_i evolves with the band; the next lemma gives the local regularity needed to treat this as smooth state dependence. The optional tangent relaxation enters only as a summable perturbation.

LEMMA 3.4 (Tangent regularity and slow-variable contribution). *Let $X_\star = (x_{1,\star}, \dots, x_{n,\star})$ be a nondegenerate MEP discretization at which the energy ordering at each interior image is strict, so that the branch of the Henkelman–Jónsson tangent mapping (2.3) is locally constant. Then $X \mapsto \tau_i(X)$ is C^1 and locally Lipschitz in a neighborhood \mathcal{K}_\star of X_\star . If the relaxed tangent defined below in (3.10) is used with $\omega_{\tau,k} \rightarrow 0$ and $\sum_k \alpha_k \omega_{\tau,k} < \infty$, then the difference between the relaxed tangent and the instantaneous Henkelman–Jónsson tangent contributes only a summable perturbation to the recursion (4.1).*

This local regularity claim is verified in Supplementary Section SM2.1. Thus the instantaneous tangent is a smooth local function of the band, and the optional tangent relaxation is absorbed by the bias term b_k in (4.1).

Lemmas 3.1 and 3.3 settle the normal-force part of the NEB iteration. The spring force controls image spacing and is measured in the same metric:

$$(3.5) \quad F_i^{\text{spring}} = k_s (\|x_{i+1} - x_i\|_{G_i} - \|x_i - x_{i-1}\|_{G_i}) \frac{\tau_i}{\sqrt{\tau_i^\top G_i \tau_i}},$$

where $\|z\|_{G_i} = (z^\top G_i z)^{1/2}$. We use the image metric G_i on both adjacent segments, which avoids midpoint covariances and keeps Algorithm 3.1 image-parallel. The frozen-metric spring mismatch is a tangential discretization error; under coupled refinement it enters the SA bias when $\sum_k \alpha_k h_{\max,k}^2 < \infty$ (see Supplementary Section SM2.3).

3.1.2. UA-NEB force. With the normal projection and spring term specified, let $\hat{g}(x_i)$ be the noisy gradient estimate of $\nabla\bar{E}(x_i)$. The UA-NEB force is

$$(3.6) \quad \mathcal{F}_i^{\text{UA}} = -Q_{\perp,G_i} G_i \hat{g}(x_i) + F_i^{\text{spring}}.$$

The first term is path-normal in the Euclidean sense; the second redistributes images along the path. If $\Sigma_F(x_i) = \sigma^2 I$, then G_i is a scalar multiple of I , the oblique

projection becomes the Euclidean normal projection, and (3.6) reduces to classical stochastic NEB up to scalar step-size and spring-stiffness rescaling. Thus (3.6) is the unpenalized UA-NEB drift.

For finite iterations one may add a transient log-determinant penalty

$$(3.7) \quad \Psi_\lambda(x) = \log \det(\Sigma_F(x) + \lambda I).$$

When Σ_F is differentiable, $\partial_{x_j} \Psi_\lambda(x) = \text{tr}[(\Sigma_F(x) + \lambda I)^{-1} \partial_{x_j} \Sigma_F(x)]$. The derivative can be evaluated by automatic differentiation, local finite differences, or the local blocks in (2.13). The image update is

$$(3.8) \quad x_i^{k+1} = x_i^k + \alpha_k \mathcal{F}_i^{\text{UA},k} - \alpha_k \gamma_k \nabla_x \Psi_\lambda(x_i^k), \quad i = 1, \dots, n.$$

For convergence to the unpenalized MEP of \bar{E} , we take $\gamma_k \downarrow 0$ with $\sum_k \alpha_k \gamma_k < \infty$. A nonzero limiting γ instead defines the regularized target $\bar{E} + \gamma \Psi_\lambda$.

3.1.3. Climbing image and tangent smoothing. After the band has relaxed close to an MEP, the highest-energy image can be converted into a UA climbing image. Let c maximize either $\bar{E}(x_i)$ or the lower-confidence score $\bar{E}(x_i) - \kappa_E \hat{\sigma}_E(x_i)$, where $\hat{\sigma}_E(x_i)$ is the ensemble standard deviation of $E^{(m)}(x_i) - E^{(m)}(a)$. Barrier reports may use the corresponding upper-confidence value $\bar{E}(x_c) + \kappa_E \hat{\sigma}_E(x_c) - \bar{E}(a)$. The UA climbing force is

$$(3.9) \quad \mathcal{F}_c^{\text{climb}} = -G_c \hat{g}(x_c) + 2Q_{\parallel, G_c} G_c \hat{g}(x_c).$$

No spring force is applied to the climbing image. The optional log-determinant penalty still enters through (3.8). The remaining images continue to use (3.8); in noisy runs, climbing is activated only after the top image is stable under the chosen energy score.

The next lemma checks the noiseless limit against the classical climbing-image dynamics.

LEMMA 3.5 (Classical-limit consistency of the UA climbing image). *Under the step-size reparametrization $\tilde{\alpha}_k := \lambda^{-1} \alpha_k$ and the limit $\Sigma_F \rightarrow 0$, $G_c \rightarrow \lambda^{-1} I$ and $Q_{\parallel, G_c} \rightarrow \tau_c \tau_c^\top / \|\tau_c\|^2$, so the deterministic UA climbing-image update reduces to the classical climbing-image iteration of [15] with effective step size $\tilde{\alpha}_k$.*

Proof. $G_c = (\Sigma_F + \lambda I)^{-1} \rightarrow \lambda^{-1} I$ as $\Sigma_F \rightarrow 0$. Substituting into (3.2) gives $Q_{\parallel, G_c} z = \tau \tau^\top z / \|\tau\|^2$, so (3.9) reduces to $\lambda^{-1} [-\nabla \bar{E} + 2(\tau \tau^\top / \|\tau\|^2) \nabla \bar{E}]$; rescaling $\alpha_k \rightarrow \tilde{\alpha}_k$ absorbs the λ^{-1} . \square

To reduce tangent noise we use the relaxed tangent

$$(3.10) \quad \tilde{\tau}_i^k = \frac{(1 - \omega_{\tau,k}) \tau_i^{k,\text{raw}} + \omega_{\tau,k} \tilde{\tau}_i^{k-1}}{\left\| (1 - \omega_{\tau,k}) \tau_i^{k,\text{raw}} + \omega_{\tau,k} \tilde{\tau}_i^{k-1} \right\|}, \quad 0 \leq \omega_{\tau,k} < 1,$$

where $\tau_i^{k,\text{raw}}$ is the energy-weighted NEB tangent (2.3). In the convergence analysis $\omega_{\tau,k} \rightarrow 0$ and $\sum_k \alpha_k \omega_{\tau,k} < \infty$ make the relaxation a transient stabilization rather than a change of the limiting tangent rule.

An optional active-learning trigger can combine pathwise covariance magnitude and directional force noise. Let \mathcal{F}_i^k denote the current UA-NEB force and $d_i^k = \mathcal{F}_i^k / (\|\mathcal{F}_i^k\| + \epsilon)$ the corresponding regularized search direction. We use, for example, (3.11)

$$\max_i \lambda_{\max}(\widehat{\Sigma}_F(x_i^k)) > \eta_{\text{var}}, \quad \max_i \frac{\sqrt{(d_i^k)^\top \widehat{\Sigma}_F(x_i^k) d_i^k}}{\|\mathcal{F}_i^k\| + \epsilon} > \eta_{\text{rel}}, \quad \widehat{\text{Var}}[\Delta E_{\text{barrier}}] > \eta_{\text{bar}}^2.$$

Algorithm 3.1 UA-NEB**Input:** Initial band, covariance estimator, and algorithm parameters.**Output:** Approximate MEP and saddle candidate.

- 1: **for** $k = 0, 1, 2, \dots$ **do**
- 2: Query ensemble forces/covariances at all images; apply $G_i^k = (\widehat{\Sigma}_F(x_i^k) + \lambda I)^{-1}$ as an operator.
- 3: Compute energy-weighted tangents τ_i^k with optional smoothing (3.10).
- 4: **for** $i = 1, \dots, n$ in parallel **do**
- 5: Apply (3.2) and (3.5) to assemble $\mathcal{F}_i^{\text{UA},k}$; use (3.9) at the climbing image once the climbing criterion is satisfied.
- 6: Set $q_i^k = \nabla_x \log \det(\widehat{\Sigma}_F(x_i^k) + \lambda I)$ if $\gamma_k > 0$ and $q_i^k = 0$ otherwise; set $s_i^k = \alpha_k(\mathcal{F}_i^{\text{UA},k} - \gamma_k q_i^k)$.
- 7: **end for**
- 8: Apply trust-radius scaling to $\{s_i^k\}$ if needed; update interior images, keep endpoints fixed, and reparametrize when spacing ratios exceed tolerance.
- 9: Stop when (4.4) and the maximum covariance score meet tolerances.
- 10: **end for**

Here $\widehat{\text{Var}}$ is the empirical ensemble variance of the barrier estimate. The first condition detects under-sampled configurations, the second detects search directions dominated by model noise, and the third controls the barrier estimate. For Dimer, the same criteria are applied to the current center and Dimer endpoints, with the reflected-gradient and rotational residuals replacing the path-image force in the reliability ratio.

Remark 3.6 (Scope of the active-learning trigger). Equation (3.11) is optional; Section 5 instead uses a matched label-refresh comparator. Its thresholds are set by force-error calibration and the desired barrier tolerance.

3.2. Uncertainty-aware Dimer. The Dimer method couples two numerical tasks with different noise profiles. The rotation of v uses a centered force difference, whose variance scales as h^{-2} in the Dimer length h (not the NEB image spacing h_i^\pm); the translation of x uses the gradient at the Dimer center. Treating these two queries with the same scalar uncertainty would miss the dominant source of rotational noise.

The geometry is also different from NEB. The Dimer translation uses the full-rank reflection $-I + 2vv^\top$, so a covariance metric cannot displace a rank-deficient zero set in the way it can for NEB. Instead, the metric damps unreliable components of the reflected-gradient translation and weights the noisy Hessian-vector residual used for rotation. We first construct the Hessian-vector covariance and Dimer length, then define the weighted rotation and translation. Throughout $\|v_k\| = 1$, with P_v as defined in the notation.

3.2.1. Hessian-vector covariance and Dimer length. For each ensemble member m , define

$$(3.12) \quad H_h^{(m)}(x)v = -\frac{F^{(m)}(x+hv) - F^{(m)}(x-hv)}{2h}.$$

The ensemble mean gives $\widehat{H}_h(x)v$ and the sample covariance gives

$$(3.13) \quad \widehat{\Sigma}_{Hv}(x, v) = s_H^2 \cdot \frac{1}{M-1} \sum_{m=1}^M (H_h^{(m)}(x)v - \widehat{H}_h(x)v)(H_h^{(m)}(x)v - \widehat{H}_h(x)v)^\top + \sigma_{H, \text{floor}}^2 I.$$

Here s_H is calibrated on reference Hessian-vector products by the same negative-log-likelihood scaling as s_{cal} in (2.11) (see Supplementary Section SM5), and $\sigma_{H,\text{floor}} > 0$ is a variance floor. In MLIP applications, these products can be obtained by centered finite differences of reference forces at $x \pm hv$ (for example DFT or a trusted classical potential), or by direct reference Hessian-vector evaluations when available. If only force covariance matrices are available, and the force evaluations at $x \pm hv$ are treated as conditionally independent, then

$$(3.14) \quad \Sigma_{Hv}(x, v) \approx \frac{\Sigma_F(x + hv) + \Sigma_F(x - hv)}{4h^2}.$$

The exact paired variance formula is given in Supplementary Section SM2.2. It specializes to (3.14) at zero correlation, while positive paired-error correlation makes (3.14) conservative.

This covariance also determines the Dimer length. If $\bar{E} \in C^4$, the centered-difference bias in (2.5) is $O(h^2)$, while independent force noise produces $O(h^{-2})$ variance. We choose the smallest h satisfying

$$(3.15) \quad \frac{\text{tr}(P_v \widehat{\Sigma}_{Hv}(x, v) P_v)}{\|P_v \widehat{H}_h(x) v\|^2 + \epsilon} \leq \eta_H,$$

subject to $h_{\min} \leq h \leq h_{\max}$.

3.2.2. Weighted rotation and translation. With a rotational covariance from (3.13) or (3.14) in hand, we can now weight the rotation step in the same way §3.1 weighted the NEB normal force. The deterministic Dimer orientation residual is

$$(3.16) \quad r_v(x, v) = P_v \nabla^2 \bar{E}(x) v.$$

It vanishes when v is an eigenvector; the local Dimer branch of interest is the lowest-curvature eigenvector selected by Rayleigh-quotient descent. We replace $\nabla^2 \bar{E}(x) v$ by $\widehat{H}_h(x) v$ and precondition the tangent residual with

$$(3.17) \quad C_v(x, v) = (P_v \Sigma_{Hv}(x, v) P_v + \lambda_H P_v)^\dagger,$$

where the pseudoinverse is taken on the tangent space $T_v \mathbb{S}^{d-1}$. A retracted rotation step is

$$(3.18) \quad \tilde{v}_{k+1} = v_k - \beta_k C_{v_k}(x_k, v_k) P_{v_k} \widehat{H}_h(x_k) v_k, \quad v_{k+1} = \frac{\tilde{v}_{k+1}}{\|\tilde{v}_{k+1}\|}.$$

The parameter $\lambda_H > 0$ bounds the angular gain; in noisy runs we also cap the rotation by a trust angle θ_{\max} .

For translation, the covariance metric acts on the reflected gradient. Unlike NEB, the Dimer translation uses a full-rank reflection rather than a rank-deficient projection. The required deterministic facts are preservation of critical points and local stability once the orientation has found the unstable mode. With $G(x) = (\Sigma_F(x) + \lambda I)^{-1}$, the UA-Dimer translation is

$$(3.19) \quad x_{k+1} = x_k + \alpha_k G(x_k) [-\hat{g}(x_k) + 2v_{k+1} v_{k+1}^\top \hat{g}(x_k)].$$

As in NEB, a transient term $-\alpha_k \gamma_k \nabla \Psi_\lambda(x_k)$ can be added. The reflection vv^\top remains Euclidean; the covariance metric preconditions only the reflected gradient. The next lemma records the two deterministic facts used later.

Algorithm 3.2 UA-Dimer

Input: x_0, v_0 with $\|v_0\| = 1$; Dimer length h ; covariance estimator; parameters $\lambda, \lambda_H, \{\alpha_k\}, \{\beta_k\}, \Delta_k, \theta_{\max}, \eta_H$.

Output: Approximate saddle x^\dagger and unstable direction v^\dagger .

- 1: **for** $k = 0, 1, 2, \dots$ **do**
- 2: Query paired ensemble forces at $x_k \pm hv_k$; form $\widehat{H}_h(x_k)v_k$ and $\widehat{\Sigma}_{Hv}(x_k, v_k)$ by (3.13) or (3.14).
- 3: If the HVP-noise ratio (3.15) exceeds η_H , enlarge h or fall back to $C_{v_k} = P_{v_k}$ and request reference labels at $x_k \pm hv_k$.
- 4: Set $\widehat{r}_v^k = P_{v_k}\widehat{H}_h(x_k)v_k$, $\delta v_k = -\beta_k C_{v_k}\widehat{r}_v^k$, capped at θ_{\max} ; retract $v_{k+1} = (v_k + \delta v_k) / \|v_k + \delta v_k\|$.
- 5: Query center force/covariance; apply the metric reflected-gradient translation, trust-radius scale it, and update x_{k+1} .
- 6: Request reference labels when (3.11) holds or $\widehat{\sigma}_{H,k}^2$ is high; stop by gradient, rotation-residual, and covariance tolerances.
- 7: **end for**

LEMMA 3.7 (Metric-preconditioned Dimer translation preserves critical points).
Let $G \succ 0$, $\|v\| = 1$, and $R_v = -I + 2vv^\top$. Define $\mathcal{T}_G(x, v) = GR_v\nabla\overline{E}(x)$. Then

$$\mathcal{T}_G(x, v) = 0 \iff \nabla\overline{E}(x) = 0.$$

Moreover, if x^\dagger is a nondegenerate index-one saddle, v^\dagger is the unstable Hessian eigenvector, and $H^\dagger = \nabla^2\overline{E}(x^\dagger)$ is positive definite on $(v^\dagger)^\perp$, then the frozen-orientation linearization

$$\dot{e} = G(x^\dagger)R_{v^\dagger}H^\dagger e$$

has all eigenvalues in the open left half-plane.

Proof. G is invertible and R_v is an involution, hence $\mathcal{T}_G = 0$ iff $R_v\nabla\overline{E} = 0$ iff $\nabla\overline{E} = 0$. At the saddle with $v = v^\dagger$, write $H^\dagger v^\dagger = \lambda_1 v^\dagger$ with $\lambda_1 < 0$ and $H^\dagger|_{(v^\dagger)^\perp} \succ 0$. Then $R_{v^\dagger}H^\dagger$ is symmetric negative definite: it keeps the negative curvature in the v^\dagger direction and reverses the positive curvatures on the orthogonal subspace. Since $G^{1/2}(R_{v^\dagger}H^\dagger)G^{1/2}$ is also symmetric negative definite and $GR_{v^\dagger}H^\dagger$ is similar to it, the linearization has real negative eigenvalues. \square

Thus the Dimer metric preconditions the reflected-gradient direction; it is not a NEB-type zero-set correction.

In Algorithm 3.2, the rotational covariance score is

$$\widehat{\sigma}_{H,k}^2 = \text{tr}(P_{v_k}\widehat{\Sigma}_{Hv}(x_k, v_k)P_{v_k}).$$

3.2.3. NEB–Dimer handoff. UA-NEB identifies the transition channel, while UA-Dimer refines a local saddle candidate.

Let c be the final climbing or highest-energy image, initialize $x_0^D = x_c^{\text{NEB}}$, and set the initial Dimer direction to the local path tangent $v_0^D = \tau_c^{\text{NEB}}$. The handoff is accepted only if the path-normal residual is small relative to its uncertainty,

$$(3.20) \quad \frac{\|Q_{\perp, G_c} G_c \widehat{g}(x_c)\|}{\sqrt{\text{tr}(Q_{\perp, G_c} G_c \widehat{\Sigma}_F(x_c) G_c Q_{\perp, G_c}^\top) + \epsilon}} \leq \eta_{\text{hand}}.$$

If (3.20) fails, the band relaxation continues or reference labels are requested near x_c . Upon acceptance, the Dimer phase normalizes v_0^D and sets

$$\Delta_0^D = \min\{\Delta_{\text{NEB}}, 2\|x_c^{\text{NEB}} - x_{c-1}^{\text{NEB}}\|\},$$

where Δ_{NEB} is the final NEB trust radius. The non-climbing band is retained only as path context.

Remark 3.8 (Scope and calibration of the handoff test). Condition (3.20) is a signal-to-noise test for seeding local refinement. By itself it does not imply membership in the Dimer stability neighborhood; the Dimer convergence statement applies once the local hypotheses of Section 4 hold.

Inexact covariance solves, trust-region tests, stopping criteria, and cached local blocks are treated as implementation perturbations. In Section 4 they enter the bias term b_k ; concrete tolerances and merit functions are recorded in Supplementary Section SM3.

4. Theory: local stochastic stability and scalable covariance. Section 3 fixed the deterministic geometry: in their mean-field limits, UA-NEB and UA-Dimer preserve the classical stationary set. The question here is whether this geometry survives stochastic implementation. We prove a local result: once the mean drift dissipates a residual, stochastic forces, covariance estimation, metric-solve errors, finite Dimer differences, and transient penalties enter as martingale noise plus summable bias, and the mean-potential residual converges to zero.

For canonical UA-NEB the required dissipative drift is verified by an explicit Lyapunov function. For UA-Dimer we identify the correct local residual near the selected index-one branch; convergence then follows from the same stochastic argument when the analogous local Lyapunov drift holds. Thus the theorem is a residual-level stability result. The analytic experiment checks its finite-time $O(1/k)$ residual prediction, while the barrier-error experiments assess whether this residual-level mechanism improves the reported saddle barrier at fixed iteration counts.

4.1. Residuals and stochastic-approximation form. Let X_k denote the full algorithmic state: for NEB, $X_k = (x_1^k, \dots, x_n^k) \in \mathbb{R}^{nd}$, while for Dimer, $X_k = (x_k, v_k) \in \mathbb{R}^d \times \mathbb{S}^{d-1}$. After projection to local coordinates on the sphere in the Dimer case, both algorithms can be written as

$$(4.1) \quad X_{k+1} = X_k + \alpha_k[h(X_k) + M_{k+1} + b_k].$$

Here h is the deterministic drift obtained by replacing stochastic forces and covariances by their conditional expectations. The term M_{k+1} is a martingale difference, and b_k collects finite-difference bias, covariance-estimation bias, regularization error, retraction error, and the transient log-determinant penalty when γ_k is summable.

For NEB, the i th component of h has the form

$$(4.2) \quad h_i^{\text{NEB}}(X) = -Q_{\perp, G_i(X)} G_i(X) \nabla \bar{E}(x_i) + F_i^{\text{spring}}(X),$$

where G_i is built from the limiting calibrated covariance. When the same force sample feeds both the gradient and the covariance, the noise splits into a force martingale, a covariance fluctuation, and a finite-ensemble bias term; independent ensemble splits or slowly updated calibration models make the martingale terms conditionally mean zero up to the bias collected in b_k .

The Dimer branch has the same SA structure, now on $\mathbb{R}^d \times \mathbb{S}^{d-1}$. To avoid confusion with the finite-difference Dimer length h , denote the Dimer deterministic vector field by d^D . In a local chart, with a fixed rotational-to-translational stepsize ratio ρ_β , the rotation and translation stack into

$$(4.3) \quad d^D(x, v) = \begin{bmatrix} G(x)r_x(x, v) \\ -\rho_\beta C_v(x, v)r_v(x, v) \end{bmatrix}, \quad \begin{aligned} r_x(x, v) &= -\nabla \bar{E}(x) + 2vv^\top \nabla \bar{E}(x), \\ r_v(x, v) &= (I - vv^\top) \nabla^2 \bar{E}(x)v, \end{aligned}$$

The implemented Dimer update differs from this drift by $O(h_{\text{dim}}^2)$ finite-difference bias and second-order retraction error bounded by the trust angle; in (4.1), $h = d^D$ for the Dimer branch.

The residuals below are the quantities controlled by the theorem. For NEB, we use

$$(4.4) \quad \mathcal{R}_{\text{NEB}}(X) = \sum_{i=1}^n \|Q_{\perp, G_i} G_i \nabla \bar{E}(x_i)\|^2 + \rho_s \sum_{i=1}^n \left| \|x_{i+1} - x_i\|_{G_i} - \|x_i - x_{i-1}\|_{G_i} \right|^2,$$

with endpoints fixed. A climbing-image residual additionally includes the reflected tangential force on the current highest-energy image. For Dimer, the residual is

$$(4.5) \quad \mathcal{R}_D(x, v) = \|(I - vv^\top) \nabla^2 \bar{E}(x)v\|^2 + \|-\nabla \bar{E}(x) + 2vv^\top \nabla \bar{E}(x)\|^2.$$

The residual is the stationarity measure; its local relation to barrier-error reporting is separated in Supplementary Proposition SM2.1.

For Dimer, the orientation component of (4.5) vanishes at any Hessian eigenvector, so the local branch is selected by the negative mode. If x^\dagger is a nondegenerate index-one saddle, v^\dagger is the normalized negative eigenvector of $\nabla^2 \bar{E}(x^\dagger)$, and the remaining eigenvalues have a positive spectral gap, then a standard perturbation argument gives, in a sufficiently small neighborhood of $(x^\dagger, \pm v^\dagger)$,

$$(4.6) \quad \begin{aligned} c_D^- \text{dist}((x, v), \{(x^\dagger, \pm v^\dagger)\})^2 &\leq \mathcal{R}_D(x, v) \\ &\leq c_D^+ \text{dist}((x, v), \{(x^\dagger, \pm v^\dagger)\})^2. \end{aligned}$$

Thus \mathcal{R}_D is the correct local residual once the Dimer phase has selected the unstable branch. To see why, write v in a local chart $v = \pm v^\dagger + \eta + O(\|\eta\|^2)$ with $\eta \perp v^\dagger$. The reflected-gradient component linearizes as $R_{v^\dagger} \nabla^2 \bar{E}(x^\dagger)(x - x^\dagger) + O(\|x - x^\dagger\|^2 + \|\eta\| \|x - x^\dagger\|)$, whose leading matrix is invertible because the saddle is nondegenerate. The orientation component linearizes in η as $(\nabla^2 \bar{E}(x^\dagger) - \lambda_1 I)\eta$ plus terms of order $O(\|x - x^\dagger\|)$, and the spectral gap between the negative eigenvalue λ_1 and the remaining eigenvalues makes this angular block invertible. The stacked residual map therefore has an invertible block-triangular linearization, modulo the sign symmetry $v \sim -v$; (4.6) then follows from the inverse function theorem. Further details are given in Supplementary Section SM2.4.

4.2. Local stability and stochastic convergence. The convergence proof needs one local deterministic input and one stochastic input: the mean drift must dissipate the residual, and the remaining terms in (4.1) must be small in the stochastic-approximation sense. We collect these requirements in a single setting.

ASSUMPTION 4.1 (Local stochastic stability setting). *Let \mathcal{R} denote the relevant squared residual, either (4.4) or (4.5). After a possible first entrance time and*

re-indexing, the iterates remain in a compact neighborhood \mathcal{K} of the target MEP discretization or saddle. On \mathcal{K} , $\bar{E} \in C^3$, $\Sigma_F \in C^1$, the covariance eigenvalues are bounded, and the deterministic drift h is locally Lipschitz. For the finite-difference Dimer bias statement below, assume in addition $\bar{E} \in C^4$.

With $\mathcal{S} = \{X \in \mathcal{K} : \mathcal{R}(X) = 0\}$, there exists a C^1 Lyapunov function V and constants $c_1, c_2, c_3 > 0$ such that

$$(4.7) \quad c_1 \mathcal{R}(X) \leq V(X) \leq c_2 \mathcal{R}(X), \quad \nabla V(X) \cdot h(X) \leq -c_3 \mathcal{R}(X)$$

on \mathcal{K} .

The noise in (4.1) satisfies

$$\mathbb{E}[M_{k+1} | \mathcal{F}_k] = 0, \quad \mathbb{E}[\|M_{k+1}\|^2 | \mathcal{F}_k] \leq C_M(1 + \|X_k\|^2),$$

and the bias is summable:

$$(4.8) \quad \sum_{k=0}^{\infty} \alpha_k \|b_k\| < \infty \quad \text{almost surely.}$$

The translational stepsizes satisfy

$$\alpha_k > 0, \quad \sum_{k=0}^{\infty} \alpha_k = \infty, \quad \sum_{k=0}^{\infty} \alpha_k^2 < \infty.$$

For Dimer, $\beta_k = \rho_\beta \alpha_k$ with fixed $\rho_\beta > 0$, up to a summable deviation. Its finite-difference bias is $O(h_k^2)$ when $\bar{E} \in C^4$, so (4.8) follows from $\sum_k \alpha_k h_k^2 < \infty$. A summable log-determinant penalty is included in b_k through the condition $\sum_k \alpha_k \gamma_k < \infty$.

For canonical UA-NEB, the local Lyapunov condition can be verified explicitly.

Canonical UA-NEB verification. Let X_\star be a nondegenerate discretized MEP. For each image, let $\tau_{i,\star}$ be the limiting energy-weighted tangent and set

$$H_i := \nabla^2 \bar{E}(x_{i,\star})|_{\tau_{i,\star}^\perp} \succ \mu_H I, \quad G_{i,\star} := (\Sigma_F(x_{i,\star}) + \lambda I)^{-1}.$$

With $y_i = Q_{\perp, G_{i,\star}}(x_i - x_{i,\star})$ and $z_i = Q_{\parallel, G_{i,\star}}(x_i - x_{i,\star})$, take

$$(4.9) \quad V(X) = \sum_{i=1}^n \left[\frac{1}{2} y_i^\top H_i y_i + \frac{\theta}{2} \|z_i\|^2 \right] + \frac{\rho_s}{2} \sum_{i=1}^n (\|x_{i+1} - x_i\| - \|x_i - x_{i-1}\|)^2.$$

PROPOSITION 4.2 (Canonical UA-NEB stability). *For suitable $\theta, \rho_s > 0$, in a sufficiently small neighborhood \mathcal{K}_\star of X_\star , the deterministic UA-NEB drift h^{NEB} in (4.2) satisfies*

$$c_1 \mathcal{R}_{\text{NEB}}(X) \leq V(X) \leq c_2 \mathcal{R}_{\text{NEB}}(X), \quad \nabla V(X) \cdot h^{\text{NEB}}(X) \leq -c_3 \mathcal{R}_{\text{NEB}}(X),$$

with constants depending on the local smoothness and spectral bounds, the constrained Hessian gap, tangent-branch separation, image-spacing lower bounds, spring stiffness, and the size of \mathcal{K}_\star . Hence the deterministic part of Assumption 4.1 holds for this canonical UA-NEB setting.

Here is the drift mechanism. Freeze τ_i and G_i at X_* and decompose $x_i - x_{i,*} = y_i + z_i$ into the Euclidean normal and metric tangent blocks used in (4.9). On the normal subspace, Taylor expansion gives $\nabla \bar{E}(x_i) = H_i y_i + O(\|X - X_*\|^2)$ after removing the tangential MEP component. The variational identity (3.4) implies, for any normal vector w ,

$$w^\top Q_{\perp, G_{i,*}} G_{i,*} w \geq c_G \|w\|^2,$$

where $c_G > 0$ is the Schur-complement lower bound of $G_{i,*}$ on $\tau_{i,*}^\perp$. Hence the normal contribution satisfies

$$\nabla_{y_i} V \cdot (-Q_{\perp, G_{i,*}} G_{i,*} \nabla \bar{E}(x_i)) \leq -c \|H_i y_i\|^2 + O(\|X - X_*\|^3).$$

The longitudinal variables are controlled by the linearized spring-spacing operator; choosing θ and ρ_s balances the normal–tangential cross terms, giving a negative definite frozen linearization. The Lyapunov spring block uses Euclidean spacings, but it is equivalent to the metric-spring residual in (4.4) because G_i and G_i^{-1} have uniformly bounded spectra. Smooth variation of $\tau_i(X)$, $G_i(X)$, and the metric spring is then absorbed by shrinking \mathcal{K}_* . The full perturbation estimates are recorded in Supplementary Section SM2.5.

The nondegeneracy hypothesis on X_* is generic when \bar{E} admits an isolated smooth continuous MEP with strictly positive constrained Hessian gap; see [31, 8] and Supplementary Section SM2.5. We work in this canonical setting for the explicit NEB stability verification. For UA-Dimer, (4.6) identifies the local residual; the same stochastic conclusion applies when the Lyapunov drift in Assumption 4.1 holds on that branch.

Assumption 4.1 gives the single estimate on which the stochastic proof rests. A Taylor expansion of V at X_k , the martingale property of M_{k+1} , the Lyapunov drift (4.7), and the second-moment bound on \mathcal{K} imply that, for sufficiently small $\sup_k \alpha_k$, there exist constants $c, C > 0$ and a summable nonnegative sequence ϵ_k such that

$$(4.10) \quad \mathbb{E}[V(X_{k+1}) \mid \mathcal{F}_k] \leq V(X_k) - c\alpha_k \mathcal{R}(X_k) + C\alpha_k^2 + \alpha_k \epsilon_k.$$

The Taylor-remainder estimates behind (4.10) are collected in Supplementary Section SM2.

THEOREM 4.3 (Local convergence). *Suppose Assumption 4.1 holds for the recursion in \mathcal{K} . Then*

$$\sum_{k=0}^{\infty} \alpha_k \mathcal{R}(X_k) < \infty \quad \text{and} \quad \mathcal{R}(X_k) \rightarrow 0 \quad \text{almost surely.}$$

Moreover, if $\mathcal{S} \cap \mathcal{K}$ consists of isolated equilibria, then X_k converges almost surely to one of them.

Proof. With $Y_k = V(X_k) + \sum_{j \geq k} C\alpha_j^2 + \sum_{j \geq k} \alpha_j \epsilon_j$, (4.10) gives $\mathbb{E}[Y_{k+1} \mid \mathcal{F}_k] \leq Y_k - c\alpha_k \mathcal{R}(X_k)$. The Robbins–Siegmund theorem [32] therefore gives convergence of $V(X_k)$ and summability of $\sum_k \alpha_k \mathcal{R}(X_k)$. The ODE method for stochastic approximation with square-summable martingale noise and summable bias [22, Thm. 5.2.1] (see also [3, Thm. 2.1]) identifies the almost-sure limit set with an internally chain-transitive set of $\dot{X} = h(X)$ inside \mathcal{K} . The strict Lyapunov drift (4.7) excludes such sets outside \mathcal{S} , hence $\mathcal{R}(X_k) \rightarrow 0$ almost surely. If $\mathcal{S} \cap \mathcal{K}$ consists of isolated equilibria, the limit component is a single point. \square

If $\gamma_k \equiv \gamma > 0$, the same proof applies after absorbing the log-determinant term into the deterministic drift. The limiting equations are then those of the regularized landscape $\bar{E} + \gamma\Psi_\lambda$ for NEB, or the corresponding regularized reflected-gradient dynamics for Dimer.

4.3. Local mean-square rate. Theorem 4.3 is qualitative. If the deterministic drift is locally linearly contractive in the Lyapunov function, the same estimate yields a non-asymptotic L^2 rate. In the canonical UA-NEB setting, Proposition 4.2 gives this contraction directly: since $V \leq c_2\mathcal{R}_{\text{NEB}}$ and $\nabla V \cdot h^{\text{NEB}} \leq -c_3\mathcal{R}_{\text{NEB}}$, one may take $\mu = c_3/c_2$.

PROPOSITION 4.4 (Local L^2 convergence rate). *Assume the setting of Theorem 4.3. Let $\mathcal{K}_\star \subset \mathcal{K}$ be a compact neighborhood of the target set on which the stronger drift inequality $\nabla V(X) \cdot h(X) \leq -\mu V(X)$ holds for some $\mu > 0$. Let $\tau_\star = \inf\{j \geq 0 : X_j \notin \mathcal{K}_\star\}$. Choose $\alpha_k = \alpha_0/(k+k_0)$ with $\alpha_0\mu > 1$ and k_0 large enough that $\alpha_k\mu \leq 1/2$. If the remainder sequence in (4.10) satisfies $\epsilon_k = O((k+k_0)^{-q})$ for some $q > 1$, then*

$$\mathbb{E}[V(X_k)\mathbf{1}_{\{\tau_\star > k\}}] = O\left(\frac{1}{k+k_0}\right)$$

and, by the equivalence of V and \mathcal{R} ,

$$\mathbb{E}[\mathcal{R}(X_k)\mathbf{1}_{\{\tau_\star > k\}}] = O(1/k).$$

If the iteration is localized so that $\tau_\star = \infty$ almost surely, this is the unconditional L^2 rate.

The proof combines (4.10) with the contraction $\nabla V \cdot h \leq -\mu V$ and a discrete Gronwall iteration [22, Ch. 2]; the full product bound and bias estimates are recorded in Supplementary Section SM2.7.

Proposition 4.4 is the rate statement checked in the analytic experiment: under the canonical setting verified in Proposition 4.2, UA-NEB has a localized $O(1/k)$ mean-square residual bound. The barrier-error experiments in Section 5 then test whether this residual-level mechanism improves the final reporting functional. For UA-Dimer, the analogous rate statement requires the local Dimer Lyapunov condition in Assumption 4.1 and the strengthened contraction hypothesis above.

Theorem 4.3 is stated for a fixed mean force and covariance model; finitely many retraining updates are handled by applying it after the last update, and continuing retraining requires summable drift perturbations (Supplementary Section SM2.8).

4.4. Scalable covariance realizations. The convergence theorem uses Σ_F only through spectral bounds and products with $G = (\Sigma_F + \lambda I)^{-1}$. It therefore does not require dense covariance matrices. The algorithms use covariance through the operator interface $z \mapsto Gz$ and scalar products involving Gz .

This interface is compatible with the standard scalable realizations used for stochastic force models. Dense covariance is useful for small validation problems but costs $O(d^2)$ storage and $O(d^3)$ factorization. Diagonal, atomwise, and local-block covariances reduce storage to $O(d)$ or $O(Nb^2)$ and make the covariance-weighted step linear in the number of local environments up to the block or Krylov cost.

Low-rank forms $\Sigma_F \approx UCU^\top$ can be applied by Woodbury with cost $O(dr + r^3)$ when the small $r \times r$ solve is factored on demand, or $O(dr + r^2)$ per apply when that factorization is cached. Crystalline-defect settings can additionally eliminate elastic far-field variables when uncertainty is localized near the defect core. Detailed

per-iteration cost models and the low-rank and far-field formulas are collected in Supplementary Section SM4.

5. Numerical experiments. The experiments follow one question: does covariance help when it is placed in the constrained update geometry? On a controlled analytic MEP, we separate metric weighting from scalar penalties and label refresh, and then check that the observed residual decay is consistent with Proposition 4.4. A covariance-rotation sweep asks when full tensor information matters. A Dimer test isolates local saddle refinement, and a W-vacancy benchmark tests path search in an atomistic defect geometry. The active-learning trigger (3.11) and the NEB–Dimer handoff condition (3.20) are not varied here.

Unless stated otherwise, \pm values are standard errors of the mean over paired stochastic seeds. Paired NEB variants share image count, iteration count, trust radii, force-evaluation counts, initial band, and force-noise sequence; the Dimer test shares initial centers, orientations, and force-query counts. Common NEB settings are identical across methods, and concrete parameter values are collected in Supplementary Section SM6 and Supplementary Table S4.

The analytic benchmark potential is

$$(5.1) \quad E(x_1, x_2) = (x_1^2 - 1)^2 + k(x_2 - a(1 - x_1^2))^2, \quad a = 0.38, \quad k = 7.5,$$

whose exact MEP is $x_2 = a(1 - x_1^2)$ and whose saddle barrier is one. We perturb the exact gradient by mean-zero Gaussian force noise whose covariance tube is placed near the transition region and whose largest eigenvector is nearly transverse to the path. This setting is simple enough to interpret geometrically and anisotropic enough to expose path wandering in Euclidean stochastic NEB.

5.1. Uncertainty-aware NEB on an analytic MEP. The finite-step NEB experiment asks where uncertainty must enter the algorithm to reduce barrier error while monitoring path deviation. Figure 1 compares six variants:

- **std**: standard stochastic NEB (Euclidean projection, no covariance);
- **pen.**: log-determinant penalty only (3.7) without metric weighting;
- **AL**: a periodic label-refresh baseline that replaces noisy forces by exact ones at the highest-uncertainty images with matched image updates; this tests uncertainty-guided labeling as a comparator, not the three-condition trigger (3.11);
- **metric**: oblique metric force (3.2) only, Euclidean spring;
- **diag**: UA-NEB with $\widehat{\Sigma}_F$ replaced by $\text{diag}(\widehat{\Sigma}_F)$, a per-component-variance ablation that isolates diagonal information from off-diagonal covariance;
- **UA**: full UA-NEB update (3.6) including the metric spring (3.5).

In the finite-step experiments we rescale each inverse-covariance metric to have trace two. This fixes the step scale; at a fixed image it leaves the oblique normal direction and its zero set unchanged.

These ablations separate uncertainty used outside the constrained update geometry (**pen.**, **AL**) from reliability placed directly in the NEB step (**metric**, **diag**, **UA**). In this base cell the high-uncertainty transition region is close enough to Cartesian alignment that diagonal weighting is expected to be a strong comparator. The rotated sweep (Figure 2) and the W-vacancy benchmark (§5.3) are designed to break this alignment.

The first conclusion is mechanistic. Only the variants that put covariance into the projected NEB step give a clear reduction in barrier error. Full UA-NEB and

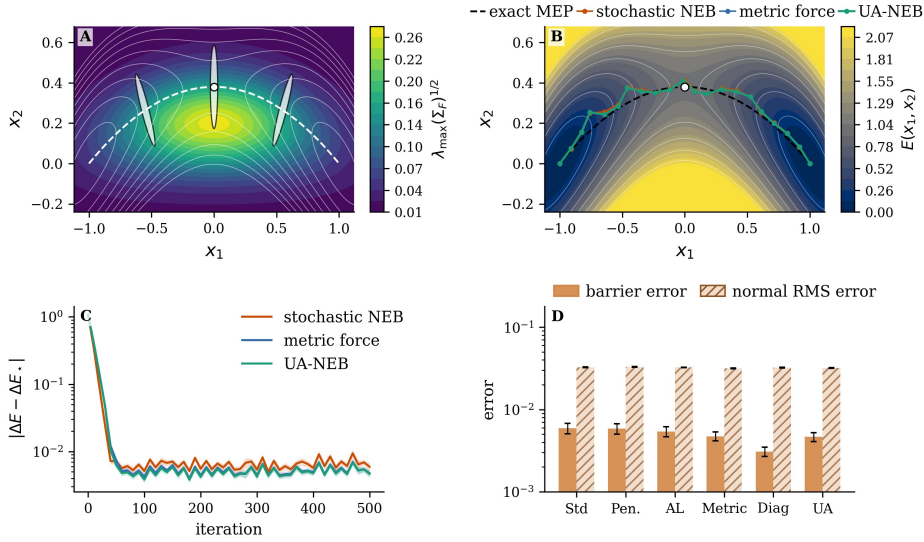


FIG. 1. *Synthetic anisotropic-noise NEB benchmark. (A) Largest force-covariance standard deviation; white ellipses show covariance eigenframes and the dashed curve is the exact MEP. (B) Representative final paths for selected methods. (C) Mean barrier-error trajectories over 200 paired seeds, with standard-error bands. (D) Final barrier error and normal-path RMS for all six ablations. Metric-based updates provide the main barrier-error gain; diagonal weighting is unusually strong in this aligned base cell, motivating the rotated-covariance sweep and W -vacancy test.*

the metric-only ablation give nearly the same improvement (about one fifth, paired Wilcoxon $p < 4 \times 10^{-5}$), whereas the scalar penalty and periodic label refresh do not change the outcome appreciably. Diagonal weighting is even stronger in this particular cell, reducing the mean barrier error by 48%, because the high-uncertainty covariance eigenframe is close to the coordinate axes. Thus the base experiment identifies the active mechanism and also explains why the diagonal realization must be carried as a necessary comparator.

The same analytic setting gives a residual-level consistency check for the theory; the supporting diagnostic is reported in Supplementary Section SM7 and Supplementary Figure S2. Over $k \in [5, 40]$, the fitted slopes range from -1.43 to -1.26 , followed by a finite-step plateau after $k \approx 50$. Its role is to check that the transient residual scale used by the theory is visible before finite-step bias dominates.

The covariance-structure sweep answers the alignment question. It rotates the principal axes relative to the path-tangent/normal frame while varying the perpendicular noise amplitude $\sigma_n^{(\text{amp})}$. Full UA-NEB improves on stochastic NEB in 22 of the 35 cells and on diagonal weighting in 20 cells. The cellwise pattern matters more than the aggregate count: diagonal weighting remains strongest near the aligned high-anisotropy corner represented by the base experiment, whereas the full tensor can gain value when reliable and unreliable directions rotate with the path. The W -vacancy benchmark below targets this non-Cartesian regime.

5.2. Dimer rotation and translation test. The Dimer experiment asks a narrower question: whether the same covariance geometry lowers the local residual floor after a path method has supplied a saddle candidate. We initialize the center away from the saddle on the analytic potential and corrupt the HVP by the same

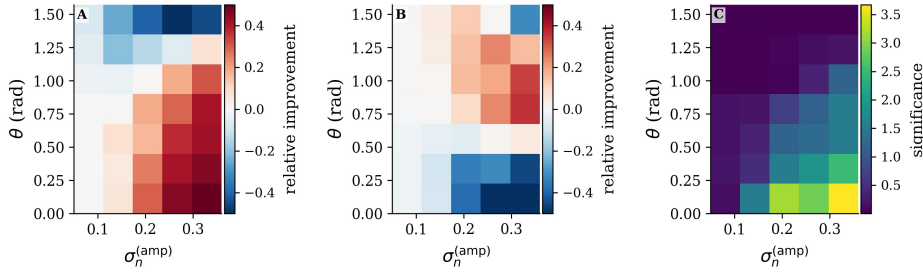


FIG. 2. Covariance-structure sensitivity sweep. (A,B) Relative improvement of full UA-NEB over stochastic NEB and diagonal weighting; positive values mean smaller barrier error, and the color scale is clipped to the displayed range. (C) Unadjusted one-sided Wilcoxon scores $-\log_{10} p$ for full UA $<$ std.

anisotropic force covariance. UA-Dimer uses the HVP covariance (3.14) in the rotation and the normalized inverse force covariance in the reflected-gradient translation. The supporting trajectories and residual distributions are shown in Supplementary Section SM8 and Supplementary Figure S3.

The result is a residual-floor improvement rather than a basin change. The mean final reflected-gradient residual drops from 0.224 ± 0.012 to 0.174 ± 0.009 (paired Wilcoxon one-sided $p < 10^{-12}$), while the distance-to-saddle success rates are 96.0% and 95.5%, respectively. Covariance weighting therefore improves local refinement before any active-learning intervention is invoked.

This local test evaluates the covariance-weighted Dimer update as a refinement mechanism for saddle candidates supplied by a path method; it does not tune the handoff threshold η_{hand} in (3.20). We do not report a separate atomistic Dimer experiment, since that would require a distinct local saddle-refinement benchmark with controlled Hessian-vector noise.

5.3. Atomistic W-vacancy benchmark. The atomistic test returns to path search under the non-Cartesian covariance structure suggested by the sweep. We test a nearest-neighbor monovacancy hop in bcc tungsten using the Mason–Nguyen–Manh–Becquart EAM/FS potential [27] as both the conditional mean force and the deterministic benchmark, with a prescribed mean-zero stochastic perturbation of covariance form (2.7). The covariance is localized near the vacancy core, strongly transverse to the hop, and coupled to an elastic far field. The deterministic reference barrier is $\Delta E_{\text{ref}} \approx 1.5379$ eV; the remaining numerical settings are listed in Supplementary Section SM6 and Supplementary Table S4.

Figure 3 is the central atomistic test for full covariance geometry. Diagonal weighting already improves the barrier estimate, but the full tensor adds the expected gain in a defect geometry whose reliable and unreliable directions are not Cartesian. The final mean absolute barrier errors are 10.14 ± 0.39 , 5.80 ± 0.14 , and 4.45 ± 0.14 meV for stochastic, diagonal, and full UA-NEB. Thus full UA-NEB reduces the mean error by 56% relative to stochastic NEB and by 23% relative to diagonal weighting. All 24 paired differences have the same sign, so the one-sided Wilcoxon tests reach their finite lower bound $p = 6.0 \times 10^{-8}$; paired Hodges–Lehmann improvements are 5.43 and 1.34 meV for the two full-UA comparisons.

The residual and rate implications are consistent with the barrier errors. The deterministic-EAM normal-force residual follows the same ordering, with full UA-NEB lowest, while panel D shows the same vacancy-hop channel across methods.

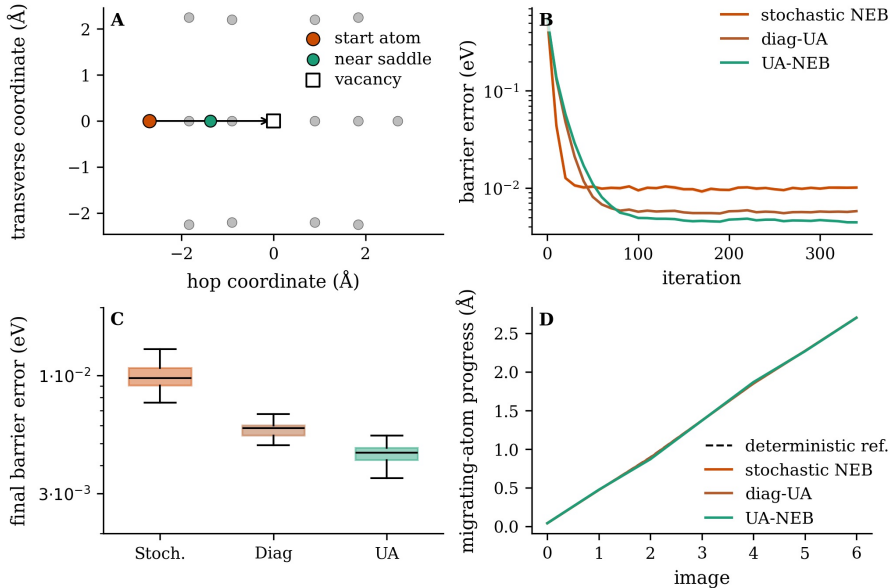


FIG. 3. Atomistic bcc tungsten vacancy-hop benchmark with EAM/FS mean force, prescribed anisotropic covariance, $N = 127$, $n = 7$, and 24 seeds. (A) Vacancy core and migrating atom. (B) Mean barrier-error trajectory. (C) Final barrier-error distribution. (D) Migrating-atom progress. Full UA-NEB reduces final barrier error by $\sim 56\%$ relative to stochastic NEB and by $\sim 23\%$ relative to diagonal weighting.

Using (2.1), the reduction in mean barrier error from 10.14 to 4.45 meV decreases the corresponding absolute rate-factor error at 600 K from about 18% to about 8%.

6. Conclusion. This paper treats anisotropic force uncertainty as part of numerical algorithm design for constrained saddle search. Rather than using covariance only to decide where to refine a surrogate, UA-NEB and UA-Dimer use it as a local metric for stochastic steps while preserving the deterministic NEB and Dimer stationarity equations. This is the sense in which the methods are geometry-preserving: uncertainty changes how an update is taken, not which mean-potential MEP or index-one saddle is targeted.

The analysis casts the iterations as Robbins–Monro recursions with controlled metric-solve bias, proves local almost-sure convergence, and gives an $O(1/k)$ L^2 residual rate under a strengthened local contraction condition. The experiments support the same algorithmic message: metric weighting, not variance avoidance alone, drives the main gains in the analytic tests, and the W-vacancy benchmark shows that full covariance information can improve over both stochastic NEB and diagonal weighting in an atomistic defect calculation. These tests isolate optimizer geometry using controlled covariance models; in deployed MLIP workflows, covariance calibration and reference-label policy remain part of the modeling pipeline. Because the metric can be realized through covariance-vector products, structured local blocks, or low-rank reductions, the approach can be coupled to ensemble or surrogate force models without changing the underlying NEB/Dimer stationary sets.

- [1] A. P. BARTÓK, M. C. PAYNE, R. KONDOR, AND G. CSÁNYI, *Gaussian approximation potentials: The accuracy of quantum mechanics, without the electrons*, Physical Review Letters, 104 (2010), p. 136403, <https://doi.org/10.1103/PhysRevLett.104.136403>.
- [2] I. BATATIA, D. P. KOVÁCS, G. N. C. SIMM, C. ORTNER, AND G. CSÁNYI, *Mace: Higher order equivariant message passing neural networks for fast and accurate force fields*, in Advances in Neural Information Processing Systems, vol. 35, 2022, pp. 11423–11436.
- [3] V. S. BORKAR, *Stochastic Approximation: A Dynamical Systems Viewpoint*, vol. 48 of Texts and Readings in Mathematics, Hindustan Book Agency and Cambridge University Press, 2008, <https://doi.org/10.1007/978-93-86279-38-5>.
- [4] H. CHEN, C. ORTNER, AND Y. WANG, *Qm/mm methods for crystalline defects. part 3: Machine-learned mm models*, Multiscale Modeling & Simulation, 20 (2022), pp. 1490–1518, <https://doi.org/10.1137/21M1441122>.
- [5] G. CUI AND K. JIANG, *Spring pair method of finding saddle points using the minimum energy path as a compass*, Physical Review E, 110 (2024), p. 064123, <https://doi.org/10.1103/PhysRevE.110.064123>.
- [6] G. CUI, K. JIANG, AND T. ZHOU, *An efficient saddle search method for ordered phase transitions involving translational invariance*, Computer Physics Communications, 306 (2025), p. 109381, <https://doi.org/10.1016/j.cpc.2024.109381>.
- [7] P. DUPUIS, M. A. KATSOULAKIS, Y. PANTAZIS, AND P. PLECHÁČ, *Path-space information bounds for uncertainty quantification and sensitivity analysis of stochastic dynamics*, SIAM/ASA Journal on Uncertainty Quantification, 4 (2016), pp. 80–111, <https://doi.org/10.1137/15M1025645>.
- [8] W. E, W. REN, AND E. VANDEN-ELINDEN, *String method for the study of rare events*, Physical Review B, 66 (2002), p. 052301, <https://doi.org/10.1103/PhysRevB.66.052301>.
- [9] S. L. FREDERIKSEN, K. W. JACOBSEN, K. S. BROWN, AND J. P. SETHNA, *Bayesian ensemble approach to error estimation of interatomic potentials*, Physical Review Letters, 93 (2004), p. 165501, <https://doi.org/10.1103/PhysRevLett.93.165501>.
- [10] N. I. M. GOULD, C. ORTNER, AND D. PACKWOOD, *A Dimer-type saddle search algorithm with preconditioning and linesearch*, Mathematics of Computation, 85 (2016), pp. 2939–2966, <https://doi.org/10.1090/mcom/3096>.
- [11] L. GUO, Y. LIU, AND T. ZHOU, *Data-driven polynomial chaos expansions: A weighted least-square approximation*, Journal of Computational Physics, 381 (2019), pp. 129–145, <https://doi.org/10.1016/j.jcp.2018.12.020>.
- [12] L. GUO, A. NARAYAN, T. ZHOU, AND Y. CHEN, *Stochastic collocation methods via ℓ_1 minimization using randomized quadratures*, SIAM Journal on Scientific Computing, 39 (2017), pp. A333–A359, <https://doi.org/10.1137/16M1059680>.
- [13] G. HENKELMAN AND H. JÓNSSON, *A dimer method for finding saddle points on high dimensional potential surfaces using only first derivatives*, The Journal of Chemical Physics, 111 (1999), pp. 7010–7022, <https://doi.org/10.1063/1.480097>.
- [14] G. HENKELMAN AND H. JÓNSSON, *Improved tangent estimate in the nudged elastic band method for finding minimum energy paths and saddle points*, The Journal of Chemical Physics, 113 (2000), pp. 9978–9985, <https://doi.org/10.1063/1.1323224>.
- [15] G. HENKELMAN, B. P. UBERUAGA, AND H. JÓNSSON, *A climbing image nudged elastic band method for finding saddle points and minimum energy paths*, The Journal of Chemical Physics, 113 (2000), pp. 9901–9904, <https://doi.org/10.1063/1.1329672>.
- [16] C. H. HO, C. ORTNER, AND Y. WANG, *Flexible uncertainty calibration for machine-learned interatomic potentials*, npj Computational Materials, (2026), <https://doi.org/10.1038/s41524-026-02080-3>. Article in press.
- [17] J. D. JAKEMAN, A. NARAYAN, AND T. ZHOU, *A generalized sampling and preconditioning scheme for sparse approximation of polynomial chaos expansions*, SIAM Journal on Scientific Computing, 39 (2017), pp. A1114–A1144, <https://doi.org/10.1137/16M1063885>.
- [18] H. JÓNSSON, G. MILLS, AND K. W. JACOBSEN, *Nudged elastic band method for finding minimum energy paths of transitions*, in Classical and Quantum Dynamics in Condensed Phase Simulations, B. J. Berne, G. Ciccotti, and D. F. Coker, eds., World Scientific, 1998, pp. 385–404, https://doi.org/10.1142/9789812839664_0016.
- [19] O.-P. KOISTINEN, V. ÁSGEIRSSON, A. VEHTARI, AND H. JÓNSSON, *Nudged elastic band calculations accelerated with Gaussian process regression based on inverse interatomic distances*, Journal of Chemical Theory and Computation, 15 (2019), pp. 6738–6751, <https://doi.org/10.1021/acs.jctc.9b00692>.
- [20] O.-P. KOISTINEN, F. B. DAGBJARTSDÓTTIR, V. ÁSGEIRSSON, A. VEHTARI, AND H. JÓNSSON, *Nudged elastic band calculations accelerated with gaussian process regression*, The Journal of Chemical Physics, 147 (2017), p. 152720, <https://doi.org/10.1063/1.4986787>.

- [21] M. KULICHENKO, K. BARROS, N. LUBBERS, Y. W. LI, R. MESSERLY, S. TRETIK, J. S. SMITH, AND B. NEBGEN, *Uncertainty-driven dynamics for active learning of interatomic potentials*, Nature Computational Science, 3 (2023), pp. 230–239, <https://doi.org/10.1038/s43588-023-00406-5>.
- [22] H. J. KUSHNER AND G. G. YIN, *Stochastic Approximation and Recursive Algorithms and Applications*, Springer, 2 ed., 2003, <https://doi.org/10.1007/b97441>.
- [23] B. LAKSHMINARAYANAN, A. PRITZEL, AND C. BLUNDELL, *Simple and scalable predictive uncertainty estimation using deep ensembles*, in Advances in Neural Information Processing Systems, vol. 30, 2017.
- [24] X. LIU, H. CHEN, AND C. ORTNER, *Convergence of the discrete minimum energy path*, 2022, <https://arxiv.org/abs/2204.07467>.
- [25] X. LIU, H. CHEN, AND C. ORTNER, *Stability of the minimum energy path*, Numerische Mathematik, 156 (2024), pp. 39–70, <https://doi.org/10.1007/s00211-023-01391-7>.
- [26] S. MAKRI, C. ORTNER, AND J. R. KERMODE, *A preconditioning scheme for minimum energy path finding methods*, The Journal of Chemical Physics, 150 (2019), p. 094109, <https://doi.org/10.1063/1.5064465>.
- [27] D. R. MASON, D. NGUYEN-MANH, AND C. S. BECQUART, *An empirical potential for simulating vacancy clusters in tungsten*, Journal of Physics: Condensed Matter, 29 (2017), p. 505501, <https://doi.org/10.1088/1361-648X/aa9776>.
- [28] D. OLSON, C. ORTNER, Y. WANG, AND L. ZHANG, *Elastic far-field decay from dislocations in multilattices*, Multiscale Modeling & Simulation, 21 (2023), pp. 1379–1409, <https://doi.org/10.1137/22M1502021>.
- [29] D. PEREZ, A. P. A. SUBRAMANYAM, I. MALIYOV, AND T. D. SWINBURNE, *Uncertainty quantification for misspecified machine learned interatomic potentials*, npj Computational Materials, 11 (2025), p. 263, <https://doi.org/10.1038/s41524-025-01758-4>.
- [30] E. V. PODRYABINKIN AND A. V. SHAPEEV, *Active learning of linearly parametrized interatomic potentials*, Computational Materials Science, 140 (2017), pp. 171–180, <https://doi.org/10.1016/j.commatsci.2017.08.031>.
- [31] W. REN AND E. VANDEN-ELJNDEN, *A climbing string method for saddle point search*, Journal of Chemical Physics, 138 (2013), p. 134105, <https://doi.org/10.1063/1.4798344>.
- [32] H. ROBBINS AND D. SIEGMUND, *A convergence theorem for non negative almost supermartingales and some applications*, in Optimizing Methods in Statistics, J. S. Rustagi, ed., Academic Press, 1971, pp. 233–257, <https://doi.org/10.1016/B978-0-12-604550-5.50015-8>.
- [33] T. TANG AND T. ZHOU, *On discrete least-squares projection in unbounded domain with random evaluations and its application to parametric uncertainty quantification*, SIAM Journal on Scientific Computing, 36 (2014), pp. A2272–A2295, <https://doi.org/10.1137/140961894>.
- [34] A. TSOURTIS, Y. PANTAZIS, M. A. KATSOLAKIS, AND V. HARMANDARIS, *Parametric sensitivity analysis for stochastic molecular systems using information theoretic metrics*, The Journal of Chemical Physics, 143 (2015), p. 014116, <https://doi.org/10.1063/1.4922924>.
- [35] J. VANDERMAUSE, S. B. TORRISI, S. BATZNER, Y. XIE, L. SUN, A. M. KOLPAK, AND B. KOZINSKY, *On-the-fly active learning of interpretable Bayesian force fields for atomistic rare events*, npj Computational Materials, 6 (2020), p. 20, <https://doi.org/10.1038/s41524-020-0283-z>.
- [36] G. H. VINEYARD, *Frequency factors and isotope effects in solid state rate processes*, Journal of Physics and Chemistry of Solids, 3 (1957), pp. 121–127, [https://doi.org/10.1016/0022-3697\(57\)90059-8](https://doi.org/10.1016/0022-3697(57)90059-8).
- [37] Y. WANG, H. CHEN, M. LIAO, C. ORTNER, H. WANG, AND L. ZHANG, *A posteriori error estimates for adaptive qm/mm coupling methods*, SIAM Journal on Scientific Computing, 43 (2021), pp. A2785–A2808, <https://doi.org/10.1137/20M1353678>.
- [38] Y. WANG, S. PATEL, AND C. ORTNER, *A theoretical case study of the generalization of machine-learned potentials*, Computer Methods in Applied Mechanics and Engineering, 422 (2024), p. 116831, <https://doi.org/10.1016/j.cma.2024.116831>.
- [39] J. YIN, B. YU, AND L. ZHANG, *Searching the solution landscape by generalized high-index saddle dynamics*, Science China Mathematics, 64 (2021), pp. 1801–1816, <https://doi.org/10.1007/s11425-020-1737-1>.
- [40] Y. YU, C. H. HO, AND Y. WANG, *A conformal prediction framework for uncertainty quantification in physics-informed neural networks*, Journal of Computational Physics, 561 (2026), p. 114979, <https://doi.org/10.1016/j.jcp.2026.114979>, <https://arxiv.org/abs/2509.13717>.